JMEPEG (2010) 19:834–840
DOI: 10.1007/s11665-009-9580-x

1059-9495/$19.00

Corrosion of Welded X100 Pipeline Steel in a Near-Neutral pH Solution

C. Zhang and Y.F. Cheng

(Submitted June 22, 2009; in revised form September 9, 2009)

In this work, electrochemical corrosion behavior of a welded X100 pipeline steel was studied in a near-neutral pH solution by electrochemical scanning vibrating electrode technique combined with metallographic and scanning electron microscopy/energy dispersive x-ray analysis. Results demonstrated that a softening phenomenon occurs around the weld, and there is the high micro-hardness in base steel adjacent to weld. In particular, there is the highest micro-hardness in base steel containing acicular ferrite and bainite. Therefore, welding and the associated post-treatment on X100 steel alter dramatically the microstructure and mechanical property around weld, resulting in an enhanced micro-hardness in base steel. There are high and low local dissolution current densities at base steel and the welded zones, respectively. The difference between the maximum and minimum dissolution current densities decreases with time, and the distribution of dissolution current density tends to be uniform. Hydrogen-charging changes the local dissolution activity of the welded steel. Different from the hydrogen-free steel, there is the highest dissolution current density at heat-affected zone. It is reasonable to assume that the charged hydrogen would accumulate at heat-affected zone, and the synergism of hydrogen and local stress results in a high anodic dissolution rate.

Keywords corrosion, micro-phase, weld, X100h pipeline steel

1. Introduction

Development of high-strength steel pipelines has provided safe and economic ways for energy transportation (Ref 1, 2). While the present high-strength steel technology has focused on improvement of strength and mechanical properties, achieving higher grades, without reducing toughness properties and weldability of the steels through thermomechanical and alloying treatments (Ref 3-5), there has been few work investigating the electrochemical corrosion behavior of high-strength line pipe steels under conditions that are relevant to pipeline operation.

Furthermore, field observations found (Ref 6, 7) that pipeline corrosion and stress corrosion cracking (SCC) frequently occurred at weld and the adjacent area. It was proposed (Ref 8-10) that welding would increase the corrosion activity and SCC susceptibility of pipeline steel due to the metallurgical changes and residual stresses introduced as well as a series of phase transformations taking place in both the weld zone and heat-affected zone (HAZ) (Ref 11). However, the exact corrosion mechanism of the welded steel has remained unclear. Minor differences in composition and microstructure between a weld metal or HAZ and the base steel could result in an electrochemical galvanic effect, affecting the corrosion behavior of the steel.

In this work, electrochemical scanning vibrating electrode technique (SVET), combined with optical and scanning electron microscopy (SEM) observation as well as electrochemical impedance spectroscopy (EIS) measurements, was used to investigate the local electrochemical corrosion behavior of the welded X100 steel in a near-neutral pH solution.

C. Zhang, Department of Mechanical and Manufacturing Engineering, University of Calgary, Calgary, AB T2N 1N4, Canada and Department of Materials Physics, University of Science and Technology Beijing, Beijing 100083, China and **Y.F. Cheng**, Department of Mechanical and Manufacturing Engineering, University of Calgary, Calgary, AB T2N 1N4, Canada. Contact e-mail: fcheng@ucalgary.ca.

2. Experimental

Test specimen was cut from a longitudinally welded X100 pipe steel containing weld metal, HAZ, and X100 base steel, as shown in Fig. 1. The chemical compositions of X100 steel and the weld metal (wt.%) are shown in Table 1. The welding was conducted by submerged arc welding. After welding, a heating treatment was maintained at least 24 h for the welded steel to avoid cracking and the formation of martensite phase. All sides of the specimen were embedded in an epoxy resin (Leco Manufacturing) except the exposure surface, which was ground sequentially with 400, 600, and 800 grit emery papers and finally polished with 3 and 1 μm diamond pastes. The specimen was cleaned by distilled water and degreased in acetone.

The test solution was NS4 solution, which has been widely used to simulate the dilute electrolyte trapped between coating and the pipeline steel (Ref 6, 7, 12, 13), with the chemical composition of 0.483 g/L $NaHCO_3$, 0.122 g/L KCl, 0.181 g/L $CaCl_2{\cdot}2H_2O$, and 0.131 g/L $MgSO_4{\cdot}7H_2O$. The solution was made from analytic grade reagents (Fisher Scientific) and ultrapure water (18 MΩ cm in resistivity). Prior to each test, the solution was purged with 5% CO_2 balanced with N_2 gas for 2 h

to achieve an anaerobic and near-neutral pH condition (pH 6.8). The gas flow was maintained throughout the test. All the tests were performed at ambient temperature.

The SVET measurements were conducted through a PAR 370 Scanning Electrochemical Workstation. The detailed set up was described in previous works (Ref 12-14). A saturated calomel electrode (SCE) was used as reference electrode and a platinum wire as auxiliary electrode. A video camera was used for imaging and controlling the distance between the Pt-Ir micro-probe and the work electrode surface, which was set at 100 μm. The vibrating amplitude of the micro-electrode was 30 μm and the vibrating frequency was 300 Hz in the direction normal to the surface. The potential of the microelectrode was proportional to its position in the vibrating plane. The difference of potentials when the microelectrode was located at the vibrating peak and valley, respectively, ΔE, was measured by an electrometer incorporated in M370. The solution resistance between the vibrating peak and valley, R, is determined by $R = d/k$, where d is the vibrating amplitude of the microelectrode (30 μm) and k is the solution conductivity. The SVET current, I, was then obtained by $I = \Delta E/R$.

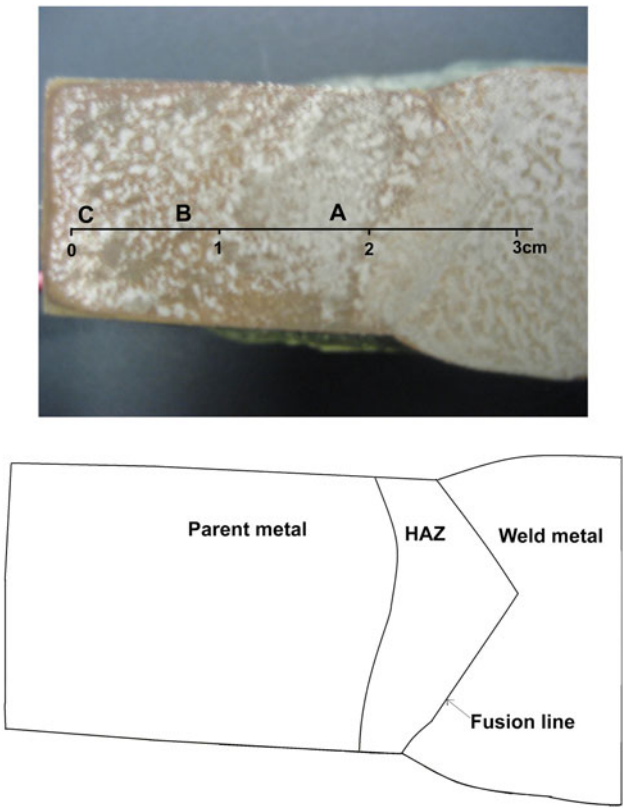

Fig. 1 Schematic diagram of the welded X100 pipeline steel specimen

Metallographic specimens of the base steel, HAZ, and weld metal were prepared by grinding and polishing with diamond paste, and etched by a mixture of 5% nitric acid and ethanol. A Philips XL30 SEM was used for metallographic observation. Micro-hardness tests were conducted through a nano-indentation measuring device (TI 900 Tribo-Indenter, Hysitron). In a force-controlled mode, the indenter tip (Berkovich type triangular pyramid) was loaded with a peak force of 3000 μN at a rate of 50 μN/s.

3. Results

3.1 Metallographic Observation and Hardness Measurement

Figure 2 shows the optical views of weld metal, HAZ, and base steel, respectively, where points A, B, and C on base steel indicate the different distances from the welding zone, as marked in Fig. 1. It is seen that various micro-phases were observed in the different zones. The weld metal was typically featured with allotriomorphic ferrite and cementite. HAZ showed a micro-phase of polygonal ferrite with an average grain size of about 10-15 μm and mixed with cementite. The microstructure of base steel was dependent on the distance form HAZ. At point A, it consisted of polygonal ferrite with an average grain size of 5-10 μm and bainite. While the micro-phase at point B was featured with acicular ferrite and granular bainite, point C consisted mainly of bainite.

The hardness measured on the specimen along the dark line in Fig. 1 is shown in Fig. 3. It is seen that there were lower values at weld metal and HAZ than those of base steel. There was the maximum hardness nearby point B in base steel.

3.2 SVET Measurement

Figure 4 shows the SVET maps measured on the welded X100 steel specimen after 1, 24, 36, and 48 h of immersion in NS4 solution, where the scanning started at point C (0 mm) and continued along the black line in Fig. 1. The scanning width was 2.4 mm. It is seen that, after 1 h of immersion, there was a maximum dissolution current density up to 120 μA/cm^2 in base steel centered at 1 cm (point B in Fig. 1), and the smallest current density of about 45 μA/cm^2 in HAZ. When the immersion time increased to 24 h, the maximum current density declined to 86 μA/cm^2, while the smallest current density in weld metal increased to 64 μA/cm^2. With the further increase of immersion time, the difference between the maximum and minimum current densities further decreased (90 μA/cm^2 versus 71 μA/cm^2 after 36 h and 64 μA/cm^2 versus 54 μA/cm^2 after 48 h of immersion, respectively). It is thus apparent that, with the increase of immersion time, the distribution of current density on the specimen tended to be uniform.

Figure 5 shows the SVET map measured on the welded X100 steel specimen immediately after hydrogen-charging at

Table 1 Chemical compositions of X100 pipeline steel (base steel) and weld metal (wt.%)

	C	Mn	S	Si	P	Ni	Cr	Mo	V	Cu	Al
X100 steel	0.07	1.76	0.005	0.1	0.018	0.154	0.016	0.2	0.005	0.243	0.027
Weld metal	0.07	1.9	…	0.42	…	2.48	0.26	0.5	…	…	…

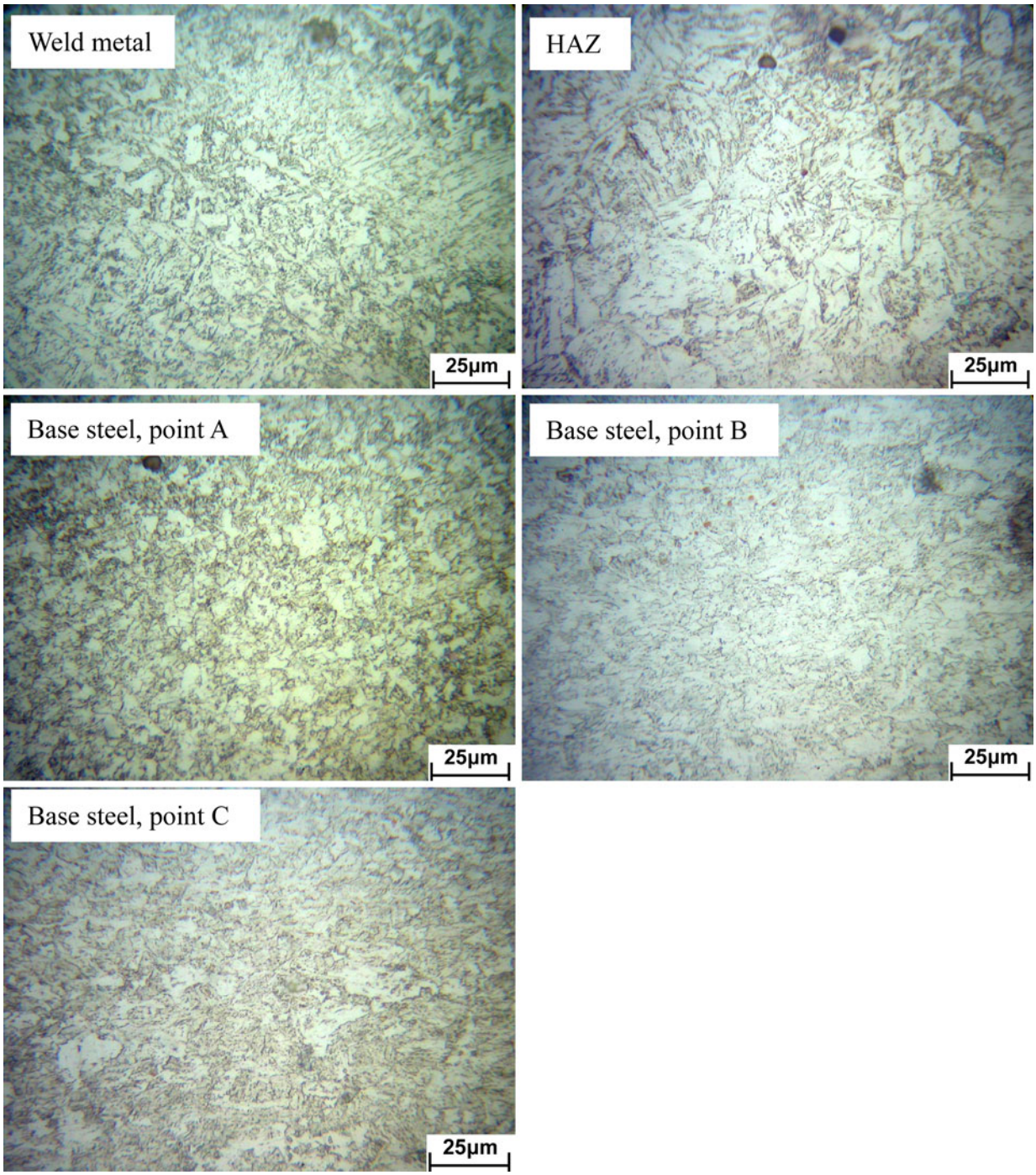

Fig. 2 Optical views of the micro-phases of welded X100 steel containing weld metal, HAZ, and different points in base steel

−2 V (SCE) for 2 h in NS4 solution in order to avoid the release of the charged hydrogen out of the steel. It is seen that there was the highest dissolution current density at HAZ.

3.3 Conventional EIS Measurements

The EIS plots measured on the macroscopic base steel electrode after 1, 24, 36, and 48 h of immersion in NS4 solution are shown in Fig. 6. It is seen that two depressed semicircles were observed on all plots. Furthermore, the size of the low-frequency semicircle increased with time.

4. Discussion

The electrochemical anodic and cathodic reactions of welded X100 steel in deoxygenated, near-neutral pH solution are oxidation of steel and reduction of water, respectively (Ref 15-17):

$$Fe \rightarrow Fe^{2+} + 2e \quad \text{(Eq 1)}$$

$$H_2O + e \rightarrow OH^- + H_{ads} \quad \text{(Eq 2)}$$

In a welded steel specimen, base steel, HAZ, and weld metal are expected to have different electrochemical dissolution

activities due to various chemical compositions and microstructures associated with the individual zone. The present work (Fig. 4) shows that there are high and low local dissolution current densities at base steel (point B) and HAZ/weld metal, respectively. Moreover, the micro-hardness measurement shows that a softening phenomenon occurs at HAZ and weld metal, as indicated in Fig. 3, and a soft allotriomorphic ferrite micro-phase in the zones (Fig. 2a, b). It is apparent that the improved microstructure and carbon distribution, which usually occurs during post-welding treatment, decrease the dissolution activity of HAZ and weld metal. It is a very important finding on welded X100 pipeline steel because the previous work (Ref 18) on welded low-grade steel, such as X70 steel, demonstrated a high dissolution current density at HAZ.

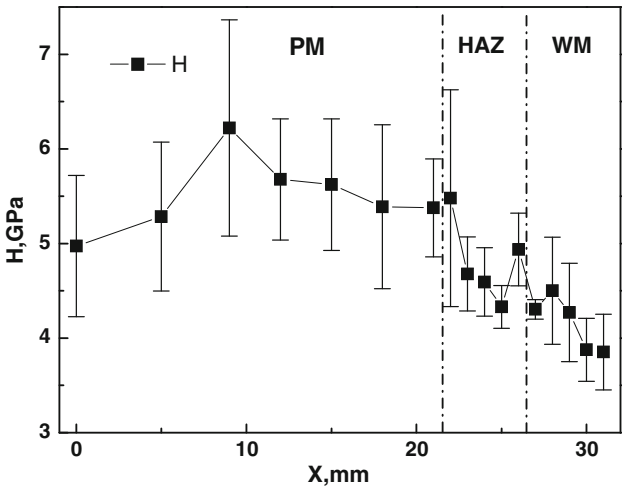

Fig. 3 Micro-hardness distribution along the line marked in Fig. 1

The micro-hardness distribution shows that, compared to the welded zones, there is a high hardness in base steel, which is associated with the presence of hardening phase of bainite. In particular, there is the highest micro-hardness at point B due to the enhancement of hardness by acicular ferrite. It is thus believed that the post-welding treatment alter dramatically the micro-structure and mechanical property around the weld, resulting in an enhanced hardness in base steel, while the as-welded structure usually contains brittle martensite phase (Ref 19).

Furthermore, point B in base steel always shows the highest current density among the various measuring points. It is mainly due to the presence of a significant amount of inclusions, i.e., the white spots, in this area, as indicated by SEM observation in Fig. 7. Previous work (Ref 20) demonstrated that the inclusions in pipeline steel are usually enriched

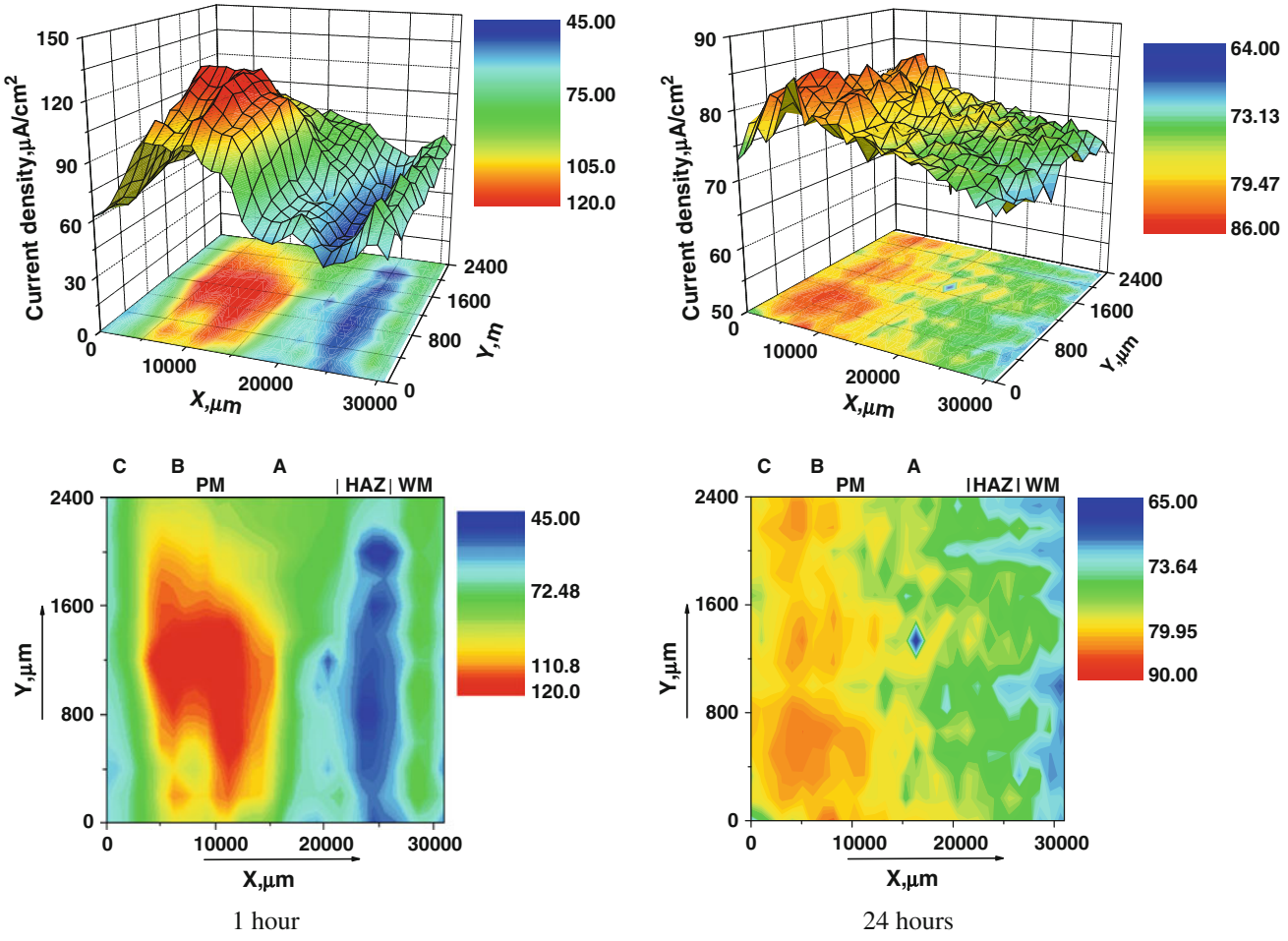

Fig. 4 SVET current density maps measured on the welded X100 steel specimen at various immersion times in NS4 solution

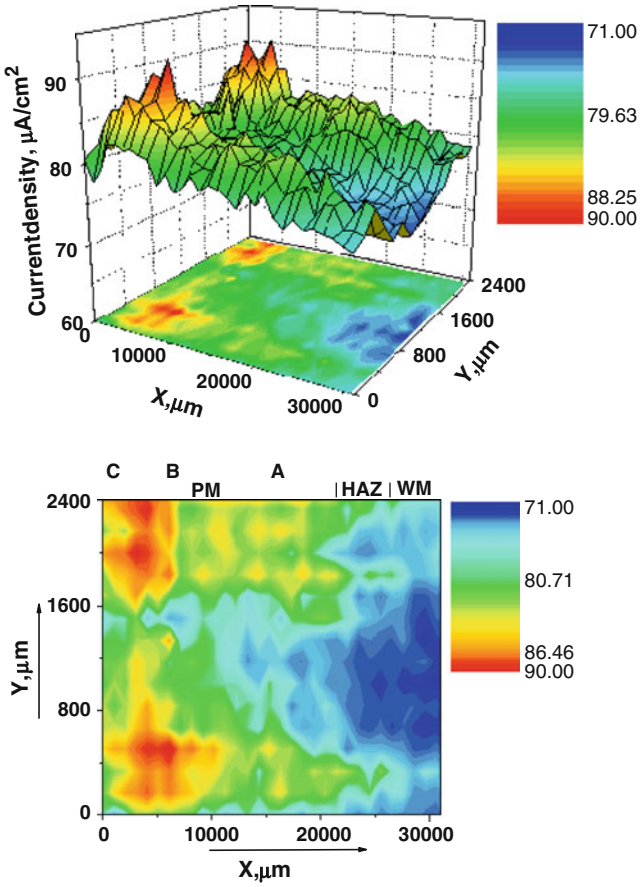

36 hours

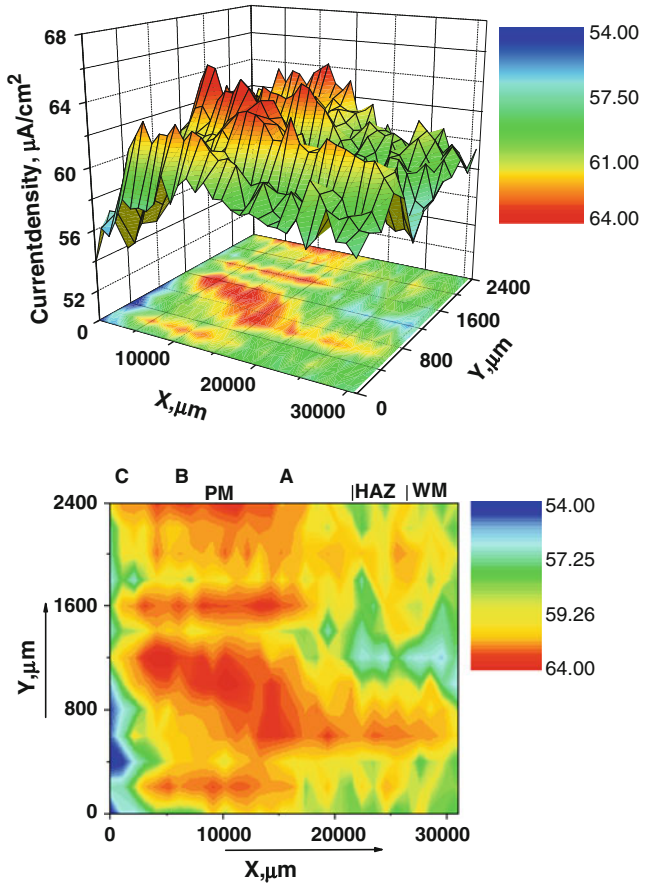

48 hours

Fig. 4 continued

in aluminum or silicon. The presence of inclusions provides local active spots for anodic dissolution. It is thus assumed that the post-welding treatment on X100 steel results in segregation of inclusions in base steel adjacent to weld, and provides potential sites for localized corrosion occurrence.

With the increase of immersion time, the difference of maximum and minimum dissolution current densities tends to be uniform on the specimen containing base steel, HAZ, and weld metal, as seen in Fig. 4. The corrosion product, mainly carbonate as demonstrated in previous work (Ref 13), forms and deposits on specimen surface, decreasing the further dissolution of steel. Moreover, once the active inclusions are dissolved away, there will be similar corrosion activities between the sites previously occupied by inclusions and other areas. It is worthy pointing out that, due to the porous structure of corrosion product deposit, serious pitting corrosion could occur under the deposit, as demonstrated in Fig. 8, which shows the electrode surface morphology after removal of corrosion product layer.

The formation of corrosion product layer and the resulting effect on corrosion of steel are also confirmed by EIS measurements in Fig. 6, where the high-frequency semicircle is associated with the corrosion product layer on electrode surface, and the low-frequency semicircle indicates the interfacial charge-transfer reaction (Ref 21). An electrochemical equivalent circuit shown in Fig. 9 is used to fit the measured impedance data, where R_s is solution resistance, CPE is constant phase element of corrosion product layer, R_1 is resistance of corrosion product layer, R_{ct} is charge-transfer resistance, and C_{dl} is double-charge layer capacitance. The fitted electrochemical impedance parameters are shown in Table 2. It is seen that, with the increase of test time, R_{ct} increases, indicating the decreasing corrosion rate of steel.

Furthermore, the present work shows that hydrogen-charging changes the local dissolution activity of the welded X100 steel. Different from hydrogen-free steel, there is the highest dissolution current density at HAZ, as seen in Fig. 5. Previous work (Ref 22) demonstrated that hydrogen-charging would enhance anodic dissolution of the steel. Therefore, it is reasonable to assume that the charged hydrogen would accumulate at HAZ.

The micro-structural characterization shows that there is no hardening phase existing in HAZ and, furthermore, the micro-hardness of HAZ is even lower than that of base steel. Thus, the hydrogen concentration at HAZ is not due to the micro-structural factor, but is probably attributed to the presence of residual stress. Zhang et al. (Ref 23) calculated the residual stress distribution caused by welding and found that the maximal longitudinal stress exists nearby the weld edge. Even after stress-relieving treatment, there is still a significant amount of residual stress existing at HAZ. Upon hydrogen-charging, the hydrogen atoms entering the steel would accumulate at sites with high stress concentration zones, such as weld (Ref 24). The synergism of hydrogen and local stress results in a high anodic dissolution rate at HAZ.

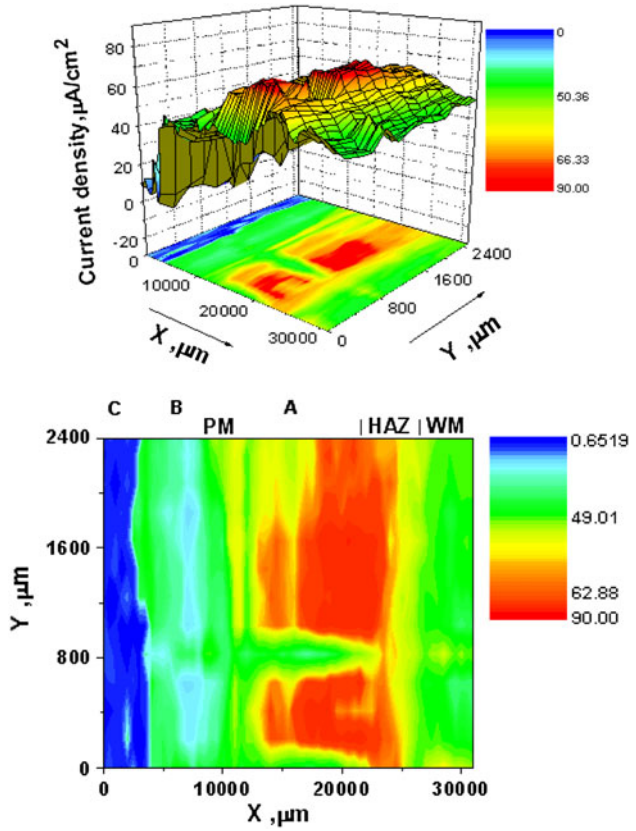

Fig. 5 SVET current density map measured on the welded X100 steel specimen after 2 h of hydrogen-charging in NS4 solution

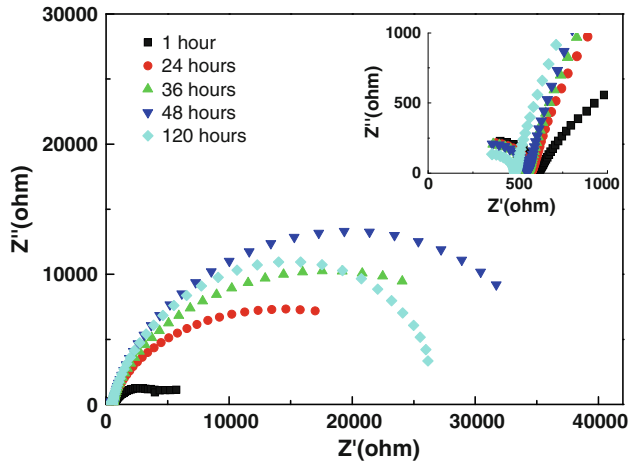

Fig. 6 Nyquist diagrams measured on a macroscopic X100 steel electrode at various immersion times in NS4 solution

5. Conclusions

A softening phenomenon occurs around weld in X100 steel due to the soft allotriomorphic ferrite microstructure generated in the zones. However, there is a high micro-hardness in base steel adjacent to weld, which is associated with the presence of hardening phase of bainite. In particular, there is the highest micro-hardness at area in base steel containing acicular ferrite.

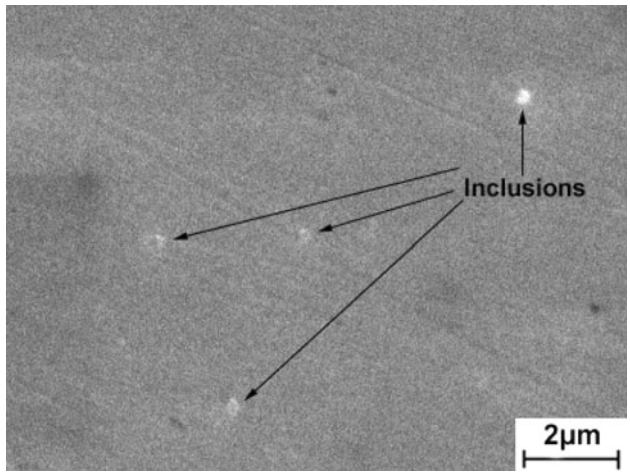

Fig. 7 Inclusions contained in X100 steel observed by SEM

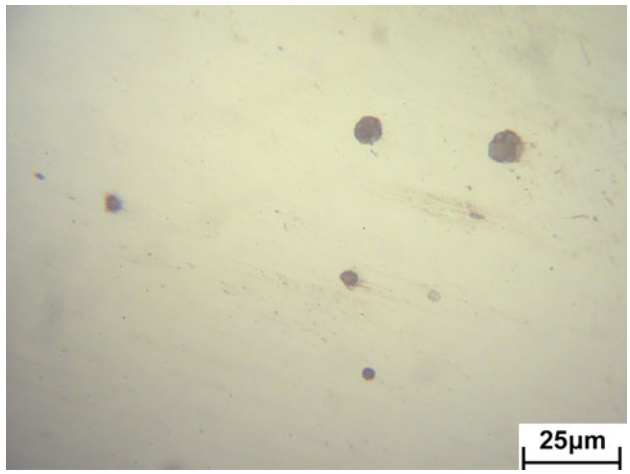

Fig. 8 The morphology of X100 steel electrode after test in NS4 solution upon removal of corrosion product

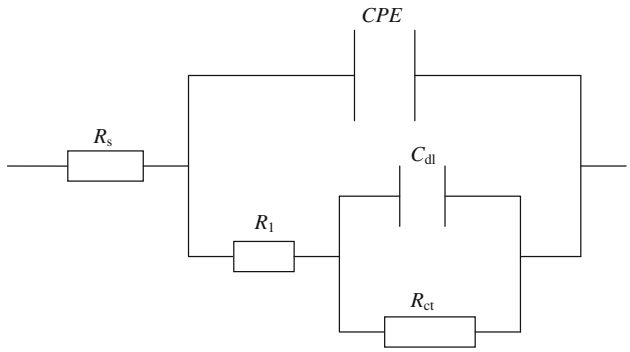

Fig. 9 Electrochemical equivalent circuit for EIS data fitting

Therefore, welding and the associated post-treatment on X100 steel alter dramatically the microstructure and mechanical property around the weld, resulting in an enhanced hardness in base steel.

There are high and low local dissolution current densities at base steel and the welded zones, respectively. With the increase

Table 2 The fitted electrochemical impedance parameters

	R_s, Ω	CPE, F	R_1, Ω	C_{dl}, F	R_{ct}, Ω
1 h	619.4	0.0006063	57.21	8.256E-6	3878
24 h	568.3	0.0002782	1335	1.739E-5	7826
36 h	542.1	0.0002936	1281	8.037E-6	2.85E4
48 h	543.8	0.0002609	585.1	1.522E-5	3.471E4

of immersion time, the difference of maximum and minimum dissolution current densities decreases, and the distribution of dissolution current density tends to be uniform on the specimen. It is attributed to the formation and deposit of corrosion product on the specimen surface, decreasing the further dissolution of steel. Moreover, once the active inclusions are dissolved away, there will be similar corrosion activities between the sites previously occupied by inclusions and other areas.

Hydrogen-charging changes the local dissolution activity of the welded X100 steel. Different from hydrogen-free steel, there is the highest dissolution current density at HAZ. It is reasonable to assume that the charged hydrogen would accumulate at HAZ, and the synergism of hydrogen and local stress results in a high anodic dissolution rate at HAZ.

Acknowledgments

This work was supported by Canada Research Chairs Program, Chinese Scholarship Council (CSC) and Natural Science Foundation of China (Project no. 50671007 and no. 50731003).

References

1. K.T. Corbett, R.R. Bowen, and C.W. Petersen, High Strength Steel Pipeline Economics, *Int. J. Offshore Pol. Eng.*, 2004, **14**, p 75–79
2. F.J. Sánchez, B. Mishra, and D.L. Olson, Magnetization Effect on Hydrogen Absorption in High-Strength Steels and Its Implications, *Scr. Mater.*, 2005, **53**, p 1443–1448
3. D. Porter, A. Laukkanen, P. Nevasmaa, K. Rahka, and K. Wallin, Performance of TMCP Steel with Respect to Mechanical Properties After Cold Forming and Post-Forming Heat Treatment, *Int. J. Press. Vess. Pip.*, 2004, **81**, p 867–877
4. H.E. Minor, A. Kifani, M. Louah, Z. Azari, and G. Pluvinage, Fracture Toughness of High Strength Steel—Using the Notch Stress Intensity Factor and Volumetric Approach, *Struct. Saf.*, 2003, **25**, p 35–45
5. Y.Z. Wang, R.W. Revie, M.T. Shehata, R.N. Parkins, and K. Krist, Initiation of Environment Induced Cracking in Pipeline Steel: Micro-Structural Correlation, *International Pipeline Conference*, ASME, Calgary, 1998
6. M. Baker Jr., Stress Corrosion Cracking Studies, Integrity Management Program DTRS56-02-D-70036, Department of Transportation, Office and Pipeline Safety, 2004
7. National Energy Board, Report of Public Inquiry Concerning Stress Corrosion Cracking on Canadian Oil and Gas Pipelines, MH-2-95, November 1996
8. S.J. Kim, M. Okido, and K.M. Moon, The Effect of Postweld Heat Treatment Affecting Corrosion Resistance and Hydrogen Embrittlement of HAZ Part in FCAW, *Surf. Coat. Technol.*, 2003, **169/170**, p 675–679
9. K.M. Moon, M.H. Lee, K.J. Kim, and S.J. Kim, Influence of Interlayers on Corrosion Resistance of Ion-Plated Mg Thin Films, *Surf. Coat. Technol.*, 2008, **202**, p 5603–5606
10. T. Hemmingsen, H. Hovdan, P. Sanni, and N.O. Aagotnes, The Influence of Electrolyte Reduction Potential on Weld Corrosion, *Electrochim. Acta*, 2002, **47**, p 3949–3955
11. W. Zhang, J.W. Elmer, and T. DebRoy, Modeling and Real Time Mapping of Phases During gta Welding of 1005 Steel, *Mater. Sci. Eng. A*, 2002, **333**, p 320–335
12. X. Tang and Y.F. Cheng, Micro-Electrochemical Characterization of the Effect of Applied Stress on Local Anodic Dissolution Behavior of Pipeline Steel Under Near-Neutral pH Condition, *Electrochim. Acta*, 2009, **54**, p 1499–1505
13. G.Z. Meng, C. Zhang, and Y.F. Cheng, Effects of Corrosion Product Deposit on the Subsequent Cathodic and Anodic Reactions of X-70 Steel in Near-Neutral pH Solution, *Corros. Sci.*, 2008, **50**, p 3116–3122
14. C.F. Dong, A.Q. Fu, X.G. Li, and Y.F. Cheng, Localized EIS Characterization of Corrosion of Steel at Coating Defect Under Cathodic Protection, *Electrochim. Acta*, 2008, **54**, p 628–633
15. R.N. Parkins, A Review of Stress Corrosion Cracking of High Pressure Gas Pipelines, *Corrosion 2000*, NACE, Houston, 2000, paper no. 363
16. L. Niu and Y.F. Cheng, Corrosion Behaviour of X-70 pipe Steel in Near-Neutral pH Solution, *Appl. Surf. Sci.*, 2007, **253**, p 8626–8631
17. Y.F. Cheng and L. Niu, Mechanism for Hydrogen Evolution Reaction on Pipeline Steel in Near-Neutral pH Solution, *Electrochem. Commun.*, 2007, **9**, p 558–562
18. C.W. Du, X.G. Li, P. Liang, Z.Y. Liu, G.F. Jia, and Y.F. Cheng, Effects of Microstructure on Corrosion of X70 Pipe Steel in an Alkaline Soil, *J. Mater. Eng. Perform.*, 2009, **18**, p 216–220
19. J. Brozda and M. Zeman, Wrong Heat Treatment of Martensite Steel Welded Tubes, *Eng. Fail. Anal.*, 2003, **10**, p 569–579
20. Z.Y. Liu, X.G. Li, C.W. Du, L. Lu, Y.R. Zhang, and Y.F. Cheng, Effect of inclusions on Initiation of Stress Corrosion Cracks in X70 Pipeline Steel in an Acidic Soil Environment, *Corros. Sci.*, 2009, **51**, p 895–900
21. E. Barsoukov and J.R. Macdonald, *Impedance Spectroscopy Theory, Experiment, and Applications*, Wiley, New Jersey, 2005
22. M.C. Li and Y.F. Cheng, Mechanistic Investigation of Hydrogen-Enhanced Anodic Dissolution of X-70 Pipe Steel and Its Implication on Near-Neutral pH SCC of Pipelines, *Electrochim. Acta*, 2007, **52**, p 8111–8117
23. H.J. Zhang, G.J. Zhang, C.B. Cai, H.M. Gao, and L. Wu, Numerical Simulation of Three-Dimension Stress Field in Double-Sided Double Arc Multipass Welding Process, *Mater. Sci. Eng. A*, 2009, **499**, p 309–314
24. R.A. Oriani, J.P. Hirth, and M. Smialowski, *Hydrogen Degradation of Ferrous Alloys*, Noyes Publications, Park Ridge, NJ, 1985